

## Effect of oxygen vacancies at the Fe/SrTiO<sub>3</sub>(001) interface: Schottky barrier and surface electron accumulation layer

P. Catrou, S. Tricot, G. Delhaye, J.-C. Le Breton, P. Turban, B. Lépine, and P. Schieffer\*  
*Université de Rennes 1, CNRS, IPR (Institut de Physique de Rennes) - UMR 6251, F-35000 Rennes, France*

 (Received 27 April 2018; revised manuscript received 10 July 2018; published 4 September 2018)

We have investigated the interface formation at room temperature between Fe and TiO<sub>2</sub>-terminated SrTiO<sub>3</sub>(001) surface using x-ray photoelectron spectroscopy. Oxygen vacancies within the SrTiO<sub>3</sub> lattice in the first planes beneath the Fe/SrTiO<sub>3</sub> interface are induced by the Fe deposition. Through a detailed analysis of the Fe 2*p*, Sr 3*d*, and Ti 2*p* core-level line shapes we propose a quantitative description of the impact of the vacancies on the electronic properties of the Fe/SrTiO<sub>3</sub> system. While for an abrupt Fe/SrTiO<sub>3</sub> junction the Schottky barrier height for electrons is expected to be about 1 eV, we find that the presence of oxygen vacancies leads to a much lower barrier height value of 0.05 eV. The deposition of a fraction of Fe monolayer also pushes the surface conduction band edge of the SrTiO<sub>3</sub> below the Fermi level in favor of the formation of a surface electron accumulation layer. This change in the band bending stems from the incorporation of oxygen vacancies in the near-surface region of SrTiO<sub>3</sub>(001). We deduce the conduction band profile as well as the carrier density in the accumulation layer as a function of the surface potential by solving the one-dimensional Poisson equation within the modified Thomas-Fermi approximation. Owing to the electric-field dependence of the dielectric permittivity, the SrTiO<sub>3</sub> with oxygen vacancies at the surface shows original electronic properties. In particular, our simulations reveal that variations of a few percent of the vacancies concentration at the surface can cause changes of several tenths of an eV in the band bending that can lead to important lateral surface inhomogeneities for the potential. We also find through our modeling that the defect states density related to oxygen vacancies at the SrTiO<sub>3</sub> surface cannot exceed, at room temperature, a critical value of  $\sim 8 \times 10^{13}/\text{cm}^2$ .

DOI: [10.1103/PhysRevB.98.115402](https://doi.org/10.1103/PhysRevB.98.115402)

### I. INTRODUCTION

Transition metal oxides with the perovskite structure have been widely investigated because of their technological importance in many applications. In particular, electric-field-induced switching of resistance in these oxides is of great interest due to their possible applications in the next generation resistance of random access memory and for computing devices [1–4]. These devices are generally composed of insulating or semiconducting structures in between two metallic electrodes that exhibit resistive switching on applying voltages. Different mechanisms have been proposed to explain the observed resistance switching effect and a large number of systems were considered till now [4]. Among them, metal/Nb-doped SrTiO<sub>3</sub>(001) junctions have been intensively studied in the last decade. Recent reports show that the resistance switching effect under high current conditions in a system such as Pt/Nb-doped SrTiO<sub>3</sub>(001) originates from a filament-type resistive switching mechanism [5] related to the oxygen-ion migration in the electric field [6]. Besides, it has been shown that the resistive switching characteristics of SrTiO<sub>3</sub>-based junctions are strongly influenced by the making process of the structures. This highlights the key role played by the structural and electronic properties as well as the interfacial morphology of such interfaces in the switching process [7].

Interfaces between polar and nonpolar perovskite oxides can also exhibit novel properties such as superconductivity [8], two-dimensional electron gas [9], and ferromagnetism [10]. As an example, a LaAlO<sub>3</sub>/SrTiO<sub>3</sub> interface can host a high mobility two-dimensional electron gas [9] which provides opportunities for the development of future nanoscale oxide-based electronic devices such as field-effect transistors [11]. It is therefore essential to control the physical properties and in particular the electrical conductivity of the two-dimensional electron gas. The basic operation to switch the electric states of the conductive channel is to apply a gate voltage between the SrTiO<sub>3</sub> and a metallic contact formed with LaAlO<sub>3</sub>. Several reports show that the metal used for the gate electrode strongly impacts the electronic properties of the LaAlO<sub>3</sub>/SrTiO<sub>3</sub>(001) system [12–14]. The work function of the deposited metal and the enthalpy of formation of the metal oxide appear as key parameters for the control of the electronic properties of this kind of system.

There is little knowledge about factors governing the Schottky barrier heights (SBHs) of metal/oxide interfaces, yet the properties of SrTiO<sub>3</sub>-based systems seems to deeply depend on the properties of the metal/oxide interfaces. In order to obtain a deeper understanding of the nature of the metal/oxide interface, we focused our attention on the electronic properties of transition metal/SrTiO<sub>3</sub>(001) junctions. Mrovec *et al.* calculated the SBH for transition metal/SrTiO<sub>3</sub>(001) abrupt junctions by first-principles density-functional theory (DFT) [15]. They found that the *n*-type SBHs typically ranged from 1.0 to 1.3 eV when

\*Corresponding author: philippe.schieffer@univ-rennes1.fr

the metal work function varies between 4.5 (Cr) and 6 eV (Pt). DFT calculations for defect-free Pt/SrTiO<sub>3</sub>(001) interfaces are in reasonable agreement with the experimental data [16,17] demonstrating that the DFT method can be used to identify the key factor that controls the SBH in transition metals/SrTiO<sub>3</sub>(001) junctions. Some experimental results do not agree with the values obtained theoretically because in such cases the metal/SrTiO<sub>3</sub> junction cannot be considered as abrupt. For example, Cr/SrTiO<sub>3</sub> junctions formed at 550 °C show an Ohmic behavior [18] which is explained by the fact that Cr atoms diffuse into the SrTiO<sub>3</sub> and occupy interstitial sites resulting in the metallization of the near-interface region [19]. In addition, there is a large dispersion in SBHs experimentally determined [17,20–24]. This points out reproducibility issues from one group to another that are related for example to the degree of cleanliness of the oxide surfaces, the substrate quality, the surface termination, or the deposition method used for making the metallic contact.

The deposition of transition metals such as Ti, Cr, Fe, and Ni on SrTiO<sub>3</sub> surfaces leads to a partial metal oxidation whose rate depends on the annealing or deposition temperature [25–31], causing possibly the creation of oxygen vacancies within the SrTiO<sub>3</sub> as this was shown with titanium [32]. These vacancies act as donor centers [33] and depending on their concentration and position, they can contribute to strongly alter the SBH value compared to the oxygen vacancies free case. DFT calculations show that adding oxygen vacancies ( $\sim 10^{14}/\text{cm}^2$ ) in the near-interface region of metal/SrTiO<sub>3</sub>(001) junctions result in the decreasing of the SBH for electrons by several tenths of an eV [34,35]. Thus far, to our knowledge, no quantitative experimental investigation was ever conducted concerning the impact of oxygen vacancies on the metal/SrTiO<sub>3</sub> SBH. In the present article we report a detailed study by x-ray photoemission spectroscopy (XPS) of the interface formation at room temperature between Fe and Nb-doped SrTiO<sub>3</sub>(001) surface in which we find that oxygen vacancies are created in the SrTiO<sub>3</sub> substrate during the interface formation. Considering the first-principle calculations available in the literature [15,34,35] we propose that the presence of oxygen vacancies explain the reduced SBH ( $\sim 0.05$  eV) for electrons that we have experimentally determined (first-principles calculations predict a SBH around  $\sim 1$  eV for an abrupt junction without any vacancies). Another interesting point revealed by our work is that the deposition of a fraction of an Fe monolayer ( $\sim 10^{15}$  atoms/cm<sup>2</sup>) pushes the surface conduction band edge of the SrTiO<sub>3</sub>(001) below the Fermi level that can yield a surface carrier accumulation layer. The surface band movement of SrTiO<sub>3</sub> observed is related to the creation of the oxygen vacancies in the near-surface region in the earliest stages of the growth. The conduction band profiles were simulated by solving the one-dimensional Poisson equation within the modified Thomas Fermi approximation (MTFA) [36]. In our modeling we have taken into account the electric-field dependence of the dielectric permittivity.

## II. EXPERIMENTAL DETAILS

The (001)-oriented SrTiO<sub>3</sub> single crystals with typical sizes of 10 mm  $\times$  10 mm  $\times$  0.5 mm were purchased from SurfaceNet. Our study was conducted using SrTiO<sub>3</sub> samples

doped with Nb at 0.015, 0.028 and 0.5 wt. % (corresponding to carrier concentrations of  $5 \times 10^{18}$ ,  $1 \times 10^{19}$ , and  $1.6 \times 10^{20}/\text{cm}^3$ , respectively) as well as undoped SrTiO<sub>3</sub> samples. In the present paper we mainly focus our discussion on the  $1 \times 10^{19}/\text{cm}^3$  doped substrate. The substrates were first annealed in air at high temperature for 1 h in order to structure the surface in atomically flat terraces as controlled by atomic force microscopy (950 °C for the Nb-doped SrTiO<sub>3</sub> and 1100 °C for the undoped SrTiO<sub>3</sub>). Then they were etched in an NH<sub>4</sub>F buffered HF solution (BHF in 7/1 volumetric ratio) for 30 s in order to obtain TiO<sub>2</sub>-terminated surfaces [37]. Finally, prior to the Fe deposition the substrates were annealed in an ultrahigh vacuum chamber (UHV system with a base pressure of  $10^{-7}$  Pa) under O<sub>2</sub> atmosphere at a pressure of 6.6 Pa and at about 650 °C for 1 h to remove any carbon contamination without affecting the oxygen stoichiometry of the substrate. The Fe layers were then deposited on the substrates in a UHV interconnected chamber by molecular beam epitaxy from an effusion cell at 1–2 ML/min [1 ML (monolayer) being defined as equivalent to the atomic surface density of Fe(001), i.e., 1 ML = 0.144 nm], below  $5 \times 10^{-8}$  Pa and on the substrates maintained at room temperature (RT). The Fe deposited amount was calibrated by a quartz microbalance. Photoemission measurements were carried out using x-ray photoelectron spectroscopy with Mg *K* $\alpha$  and Al *K* $\alpha$  as sources and the spectra were recorded at RT. A two-axis manipulator allowed polar and azimuthal sample rotations (the polar angle  $\theta$  is defined with respect to the surface normal). The kinetic energy of the emitted electrons was measured by employing a hemispherical analyzer (Omicron EA125) with a five-channel detection system, an energy resolution better than 0.9 eV, and an angular resolution of  $\sim 1^\circ$ . The Au 4*f*<sub>7/2</sub> peak position from a thick gold sample, assumed to be 84.00 eV binding energy [38], was taken as a reference in order to position the Fermi level. In our experiments the binding energy of the energy levels was measured with respect to the Fermi level of the sample. No evolution of the shape, energy position, or intensity of the photoemission spectra was observed during the photoemission experiments showing that no aging effect took place during the data acquisition.

## III. RESULTS

### A. Epitaxial growth of Fe

The TiO<sub>2</sub>-terminated SrTiO<sub>3</sub>(001) surface shows an intense  $1 \times 1$  reflection high-energy electron diffraction (RHEED) pattern. During the Fe growth the initial SrTiO<sub>3</sub> RHEED pattern, progressively fades into an increasing background with the persistence of the  $1 \times 1$  pattern up to  $\sim 2$  ML Fe suggesting that in this coverage range the overlayer continuously covers the substrate. Diffraction features of the Fe overlayer appear around 4 ML Fe. Their intensity then increases progressively as more Fe is deposited (as shown in Fig. 1 for a 10 ML Fe thickness). By indexing the diffraction patterns we deduce that Fe grows mainly in the body centered cubic (bcc) structure with the epitaxial relationship Fe(001)[100]//SrTiO<sub>3</sub>(001)[110]. The same epitaxial relationship was found for Fe layers deposited onto SrTiO<sub>3</sub>(001) at RT [39] or at higher temperature ( $\sim 473$  K) [40]. The shape

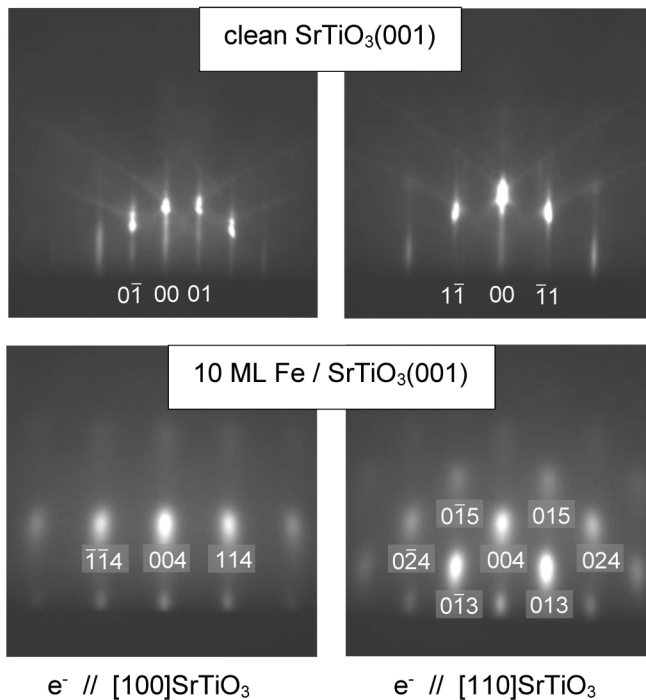


FIG. 1. RHEED patterns along the [100] and [110] SrTiO<sub>3</sub> azimuths of a clean SrTiO<sub>3</sub>(001) surface and of a 10 ML Fe film grown on SrTiO<sub>3</sub>(001) (Miller indices are labeled below the diffraction spots or streaks).

of the diffraction spots of the bcc Fe pattern also indicates that the surface of the film is rough (up to 35 nm, the largest Fe thickness deposited on SrTiO<sub>3</sub>) in agreement with the scanning tunneling microscopy (STM) studies performed by Chien *et al.* [41].

### B. Interface reactivity

Figure 2 shows Al  $K\alpha$  excited Fe 2*p* core-level photoemission spectra (normalized to their own maximum value and vertically shifted for clarity) at normal emission for several Fe thicknesses, pure Fe and an FeO layer. The Fe 2*p* core-level spectra show two main peaks that correspond to the spin-orbit doublet (Fe 2*p*<sub>3/2</sub> at ~707 eV and Fe 2*p*<sub>1/2</sub> at ~720 eV). The small structures that appear at binding energies between ~693 and ~703 eV are contributions originating from x-ray satellite replicas of the nonmonochromatized source. At 10 ML Fe, the spectrum is fitted with the pure metal experimental curve. For the lowest coverages, the spectra are dominated by the metal contribution with an asymmetric widening of the main structures towards higher binding energies. This indicates the presence of an additional Fe 2*p* component located, from a rough analysis, at about 2.7 eV from the main component. Considering the relative position of the Fe 2*p*<sub>3/2</sub> core level of FeO, Fe<sub>2</sub>O<sub>3</sub>, and Fe<sub>3</sub>O<sub>4</sub> to that of the Fe metal we propose that this component is due to electron emission from Fe in an FeO phase [42,43]. It can be noted that no trace of oxidized species is detected for 1 ML of Fe deposited on GaAs(001) in the same experimental conditions as in the present work [44] proving that the oxygen atoms involved in the FeO come from the SrTiO<sub>3</sub> substrate rather than from the residual gas

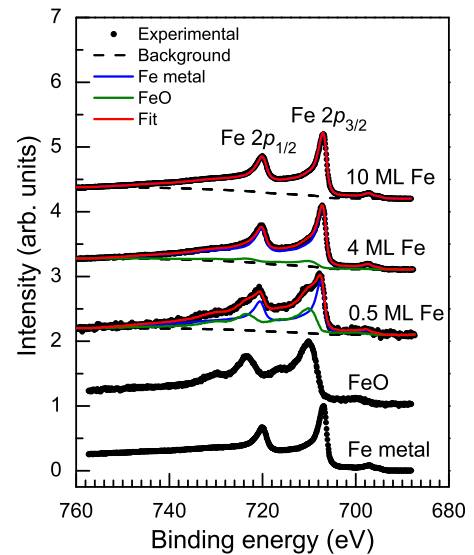


FIG. 2. Fe 2*p* core-level experimental spectra and line shape decomposition for 0.5, 4, and 10 ML of Fe deposited at RT on TiO<sub>2</sub>-terminated SrTiO<sub>3</sub>(001) surface. The experimental spectra were collected at normal emission and at a photon energy of 1486.6 eV. The two bottom curves are reference spectra for FeO and metallic Fe taken in the same conditions as above. These spectra were used in the fitting procedure.

atmosphere. We will see in the following from the analysis of the line shape of the Ti 2*p* core-level spectra that oxygen atoms involved in FeO are indeed released from the substrate during the Fe/SrTiO<sub>3</sub> interface formation.

For a more quantitative analysis, we have performed Fe 2*p* core-level line shape decomposition with a least-square fitting procedure using pure Fe and FeO reference spectra, which were respectively recorded on a 10-nm-thick iron layer and on a 0.4-nm-thick FeO layer. Line shape decompositions are superimposed to experimental data. The FeO layer was obtained by the deposition of one monolayer of Fe on SrTiO<sub>3</sub>(001) at RT followed by an exposure to  $1 \times 10^3$  Langmuir of molecular oxygen giving an Fe 2*p* core-level spectrum that strongly resembles that of Fe<sub>2</sub>O<sub>3</sub>. Then, the deposition of ~0.5 ML at RT converts the Fe<sub>2</sub>O<sub>3</sub> in FeO [42,45]. The analysis of the evolution of the intensity of the FeO component as a function of the Fe thickness shows that the partial oxidation of Fe takes place in the early stage of the growth and that the amount of oxidized iron slightly increases up to Fe depositions of 4–6 ML. Then increasing Fe coverage leads to a decreasing of the FeO intensity showing that the oxide is buried under the additional deposited iron. The density of oxidized iron atoms per surface unit deduced from our analysis (assuming a homogeneous distribution of the oxidized atoms within the overlayer) is about  $\sim 2 \times 10^{14}/\text{cm}^2$ . This value is 6 times lower than the atomic density of the Fe(001) surface demonstrating that a limited reaction occurred at the Fe/SrTiO<sub>3</sub> interface.

In Fig. 2, as compared with the bulk Fe, the Fe 2*p* metal component for 0.5 ML Fe/SrTiO<sub>3</sub>(001) is shifted by 0.5 eV towards higher binding energies. We observe that this shift progressively decreases when increasing the Fe coverage up

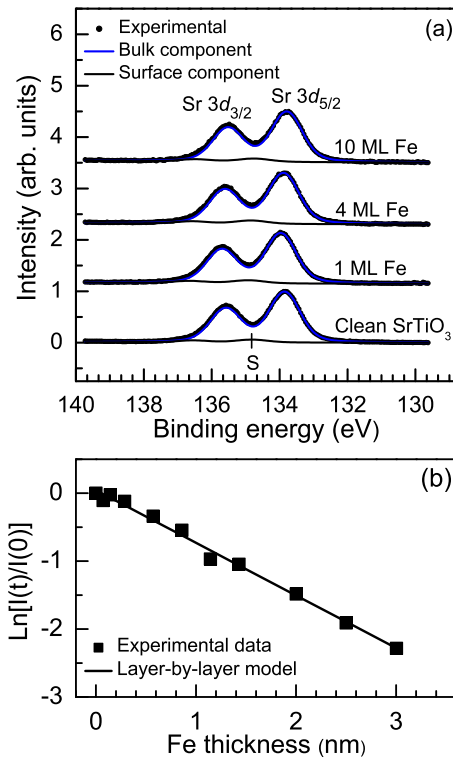


FIG. 3. (a) Sr  $3d$  core-level experimental spectra and line shape decomposition for various Fe coverages. The experimental spectra were collected at normal emission and at a photon energy of 1253.6 eV. The component labeled S is assigned to an electron emission from SrO patches at the SrTiO<sub>3</sub>(001) surface or at the Fe/SrTiO<sub>3</sub>(001) interface. (b) Evolution of the bulk component of the Sr  $3d$  core-level experimental intensity [where  $I(t)$  is the integrated intensity at thickness  $t$ ] plotted in semilogarithmic scale as a function of the Fe coverage (full square). The integrated intensity was obtained by integrating the photoemission intensity (that is in counts per second) over the whole spectrum. The fitted substrate attenuation for a layer-by-layer growth mode (continuous line) is also presented.

to becoming negligible above 10 ML. This effect is neither directly related to the band bending effect in oxides nor to work function changes of the system but it could come from a final state effect in photoemission. Such an effect is induced by the presence of a photohole remaining on the metal islands during the photoemission process. It was observed for gold clusters formed on SrTiO<sub>3</sub>(001) surfaces [46]. However, as long as we do not know the morphology of the Fe films in the early stages of growth, it is difficult to quantify this final state effect.

### C. Schottky barrier

Figure 3(a) presents Sr  $3d$  core-level spectra (normalized to their own maximum value and vertically shifted for clarity) taken at normal emission and excited with Mg  $K\alpha$  radiation for different Fe thickness deposited onto SrTiO<sub>3</sub>(001) at RT. The experimental spectra were decomposed after background correction with a least-square procedure using a Lorentzian convoluted with a Gaussian to represent each spin-orbit-split component of the Sr  $3d$  core level. In the fitting procedure

the spin-orbit splitting of the Sr  $3d$  core level was fixed at 1.74 eV [47] and the branching ratio was taken to be the statistical value of 3:2. For the clean surface, the spectrum is dominated by the well resolved spin-orbit doublet (Sr  $3d_{5/2}$  at 133.8 eV and Sr  $3d_{3/2}$  at 135.6 eV). To obtain satisfactory fits we had to include an additional component S located  $\sim 1.0$  eV higher than the main component binding energy for every Fe coverage. By comparing the intensity of each component at normal emission and at a more surface sensitive emission angle we found that the S component is related to a surface contribution. In previous studies, based on photoelectron diffraction [48], atomic force microscopy (AFM) [49,50], and medium energy ion scattering [51], it was proposed that this additional component can be related to Sr atoms at the surface (the Sr atoms can segregate at the substrate surface during the thermal treatment). From there we consider that the surface component S that occurs during the annealing process under O<sub>2</sub> atmosphere is associated with the formation of SrO clusters at the surface or the development of SrO terraces. Considering our oxidizing experimental conditions it is unlikely that the surface component S is related to some Sr adatoms randomly distributed on the surface. From the quantitative analysis of photoemission intensities we found that these SrO patches at the surface cover less than 25% (10%) of the surface if their height is of one (three) atomic SrO layer. It can be noted that immediately after the chemical etching before the last *in situ* treatment (annealing under O<sub>2</sub> atmosphere) there is no additional component in the XPS spectra of the Sr  $3d$  core level, meaning that the treatment with the NH<sub>4</sub>F buffered HF solution is sufficient enough to yield a pure TiO<sub>2</sub>-terminated surface.

Figure 4(a) shows the morphology of the SrTiO<sub>3</sub>(001) surface obtained by atomic force microscopy before the Fe deposition (after the *in situ* annealing of SrTiO<sub>3</sub> under an O<sub>2</sub> atmosphere at a pressure of 6.6 Pa). The image was

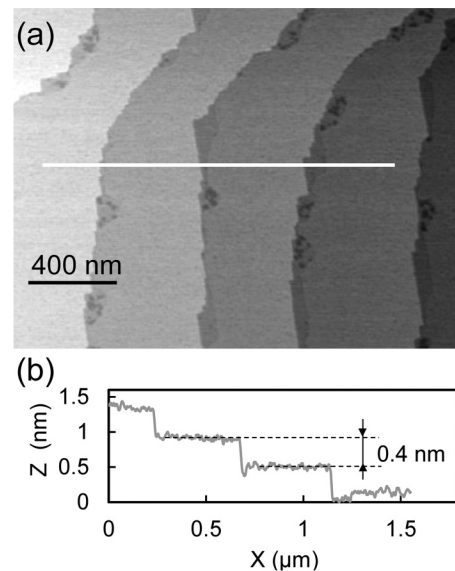


FIG. 4. (a) AFM height image of a clean TiO<sub>2</sub>-terminated SrTiO<sub>3</sub>(001) surface. (b) Height profile along the white line on the AFM image.

obtained in air for an undoped sample and conducted in tapping mode. Atomically flat terraces of several hundred nanometers in width separated by  $\sim 0.4$  nm high steps corresponding to one unit cell of SrTiO<sub>3</sub> [Fig. 4(b)] can be observed. Considering our experimental protocol as well as the XPS results we conclude that the flat terraces correspond to TiO<sub>2</sub>-terminated surface regions [37]. It can be also seen in Fig. 4(a) perturbed regions along the step edge that extend on several tens of nanometers in the direction perpendicular to the steps. Such morphological features were observed by Bachelet *et al.* [52] and assigned to SrO trenches. In our case these SrO-terminated regions occupy  $\sim 10\%$ – $20\%$  of the surface and could explain the presence of the S component in the Sr 3*d* core-level photoemission spectra. Note that the spatial resolution of our atomic force microscope is probably insufficient to observe disordered SrO islands at the substrate surface [53]. Further experimental investigations are still needed to unambiguously determine the origin of the S component.

The line shape of the Sr 3*d* core-level spectra does not change with increasing the Fe coverage showing that the Sr cations chemical environment remains unchanged during the Fe deposition. This indicates that the Fe atoms do not form an interfacial alloy with Sr atoms. Upon the Fe deposition we observe small nonmonotonic variations in the binding energy (0.2–0.3 eV) that are caused by band bending changes in the SrTiO<sub>3</sub> during the interface formation. This will be discussed later in the paper. In Fig. 3(b) we have plotted in semilogarithmic scale the intensity of the main component as a function of the Fe thickness. This component is attenuated with a  $1/e$  decay of  $\sim 1.3$  nm, a value close to the effective attenuation length of 1.4 nm for photoelectrons of kinetic energy  $\sim 1.12$  keV [54] and for a layer-by-layer model [full line in Fig. 3(b)]. The same observation is also done for the S component. These behaviors show that Fe wets the SrTiO<sub>3</sub>(001) surface relatively well, confirming our RHEED analysis. In addition to this, STM measurements [41] show that for 10 ML Fe, the films completely cover the SrTiO<sub>3</sub> surface at RT. Hence we conclude that the Fe/SrTiO<sub>3</sub> interface is formed during the deposition of the first 10 ML Fe.

We have not taken into account the Fe layer roughness in our photoemission intensity analyses of the Sr 3*d* core level because the photoemission intensity attenuation shown in Fig. 3(b) is weakly sensitive to the presence of a film surface roughness. According to the STM study of 10 ML Fe/SrTiO<sub>3</sub> performed by Chien *et al.* [41] the surface roughness of the Fe films (given by the peak-to-valleys height taken from an STM profile) is  $\sim 0.8$  nm. We have introduced this roughness parameter in a one-dimensional sinusoidal model [55] to quantify the impact of the film surface roughness on the substrate photoemission intensity attenuation by the Fe film. We find that for 10 ML of Fe the substrate photoemission intensity at normal emission with the surface roughness deviates by less than 3% from that expected for a layer-by-layer model. This difference is not detectable within our experimental sensitivity. More generally, our simulations show that a significant deviation (higher than 5%) appears only when the peak-to-valley height is higher than the effective attenuation length ( $\sim 1.4$  nm).

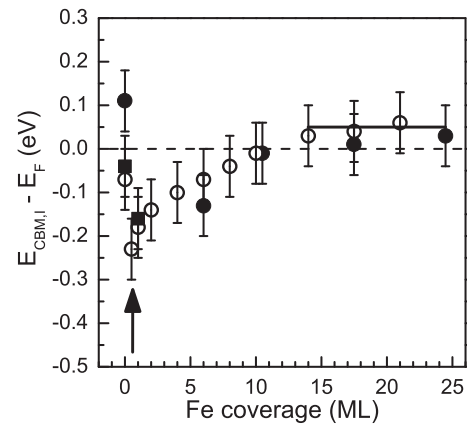


FIG. 5. Evolution of the position of the conduction band edge ( $E_{CBM,1}$ ) relative to the position of the Fermi level ( $E_F$ ) at the Fe/SrTiO<sub>3</sub> interface as a function of the Fe coverage. The different symbols correspond to measurements performed with different samples with the same *n*-type doping concentration of  $1 \times 10^{19}/\text{cm}^3$ . These data were obtained from the position of the Sr 3*d*<sub>5/2</sub> core level. The extracted values were not corrected by the band bending. The arrow indicates the minimum value of the curve that appears after the deposition of  $\sim 1$  ML Fe.

Figure 5 shows the evolutions of the position of the conduction band edge ( $E_{CBM,1}$ ) relative to the position of the Fermi level ( $E_F$ ) at the Fe/SrTiO<sub>3</sub> interface as a function of the Fe coverage for several substrates with the same doping concentration. These results are derived from the Sr 3*d*<sub>5/2</sub> core-level binding energy (extracted from XPS spectra at normal emission) of the main component using a band gap energy for SrTiO<sub>3</sub> of 3.25 eV [56] and an energy separation of 130.54 eV between the valence band maximum of SrTiO<sub>3</sub> and the Sr 3*d*<sub>5/2</sub> core-level position [57]. For the moment, the results presented in Fig. 5 are not corrected by the band bending. The curves for the different samples show the same nonmonotonic behavior with a marked minimum for Fe coverages of  $\sim 1$  ML. For the clean SrTiO<sub>3</sub>(001) the conduction band edge at the surface is very close to the Fermi level. The deposition of the fraction of an Fe monolayer pushes the surface conduction band edge of the SrTiO<sub>3</sub> fairly far below the Fermi level indicating that Fe deposition (1 ML Fe) induces a metallization of the SrTiO<sub>3</sub>(001) surface. Then, as the Fe coverage increases, the conduction band edge progressively shifts towards the Fermi level during the interface formation and does not move for coverages higher than 10–15 ML. We can therefore conclude that when the Fe/SrTiO<sub>3</sub>(001) barrier is formed, the Fermi level is located  $\sim 0.05$  eV below the conduction band edge at the interface that corresponds to a SBH for electrons of  $0.05 \pm 0.07$  eV. In this case the band bending affects the position of the Sr 3*d* core-level position by less than 0.02 eV. Experiments carried out with doping concentrations of  $5 \times 10^{18}$  and  $1.6 \times 10^{20}/\text{cm}^3$  or with an undoped sample lead to similar values for the SBH. To complete this study we have conducted current-voltage measurements with 55-nm-thick iron contacts of 500  $\mu\text{m}$  in diameter deposited *in situ* at RT using shadow masks on the *n*-doped SrTiO<sub>3</sub>(001) with a doping concentration of  $\sim 5 \times 10^{18}/\text{cm}^3$ . We found that the Fe/SrTiO<sub>3</sub> contact is Ohmic

suggesting that the SBH is very low as this was found for metal/SrTiO<sub>3</sub> contacts formed with reducing metals such as Al, Ti, or Cr [18,23]. The analysis of the differential resistance around zero bias for temperatures between 200 and 300 K through the thermionic emission theory provides a SBH value lower than 0.25 eV in agreement with our photoemission results.

Let us now compare our results with the theoretical prediction carried out within the DFT framework for abrupt transition-metal/SrTiO<sub>3</sub>(001) junctions [15]. In this theoretical work the Fe/SrTiO<sub>3</sub> contact was not studied, however, chromium that was considered in this theoretical study has a very similar work function and the same crystalline structure than iron. Thus we expect that Fe/SrTiO<sub>3</sub> and Cr/SrTiO<sub>3</sub> systems for abrupt interfaces share similar SBHs. We therefore assume from the DFT calculation that for an abrupt Fe/SrTiO<sub>3</sub>(001) interface the SBH must be of  $\sim 1.3$  eV (1.0 eV) for TiO<sub>2</sub>(SrO)-terminated SrTiO<sub>3</sub>(001) systems. Given that iron is deposited on a substrate with a mixed terminated surface (10%–20% of the surface is SrO-terminated) and considering these DFT predictions [15] which show that the SBH depends little on the nature of the SrTiO<sub>3</sub> surface termination, we conclude that the mean value of the SBH for an abrupt Fe/SrTiO<sub>3</sub> interface with a mixed termination should be around 1 eV with a standard deviation of some tenths of an eV. This result is in complete disagreement with our experimental observations. However, if we remember that oxygen atoms are released from the SrTiO<sub>3</sub> substrate during the Fe/SrTiO<sub>3</sub> interface formation we can explain this fact. Indeed, oxygen atoms expelled from the substrate during the interface formation leave behind oxygen vacancies and as demonstrated by first-principle calculations these vacancies in the near-interface region can lead to a decrease of the SBH [34,35].

It can be interesting to note that chromium also forms an Ohmic contact with *n*-type SrTiO<sub>3</sub>(001) [18]. This was observed for Cr/SrTiO<sub>3</sub>(001) junctions formed at 550 °C and assigned to the chemically nonabrupt character of the interface. More precisely, some chromium atoms diffuse into the SrTiO<sub>3</sub> lattice occupying the interstitial sites resulting in the metallization of the near-interface region as experimentally observed and revealed by first-principles calculations [19]. A nonabrupt interface was also observed for the Fe films formed at 550 °C on an *n*-type SrTiO<sub>3</sub>(001) surface, but in this case the junctions shown a rectifier character with a SBH of  $\sim 0.5$  eV [30]. According to the works of Chambers *et al.* [30] at high temperature some Fe atoms diffuse into the SrTiO<sub>3</sub> lattice but occupy the titanium sites in the SrTiO<sub>3</sub> lattice. Clearly these results differ from that shown in the present study because the Fe/SrTiO<sub>3</sub> junctions formed at RT show an Ohmic character.

#### D. Interface formation: Creation of oxygen vacancies

Further information about the interface chemical properties can be obtained from the analysis of the line shape of the Ti 2*p* core-level photoemission spectra [58]. Figure 6(a) shows the Al *K* $\alpha$  excited Ti 2*p* core-level spectra for 0, 0.5, and 4 ML Fe. The clean surface spectrum is dominated by the well-resolved spin-orbit doublet (Ti 2*p*<sub>1/2</sub> at 465.0 eV and Ti

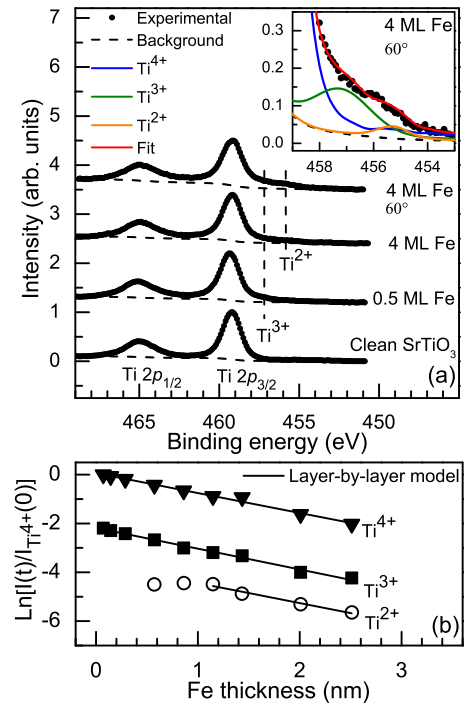


FIG. 6. (a) Ti 2*p* core-level experimental spectra for various Fe coverages. The experimental spectra were collected at a photon energy of 1486.6 eV and at normal emission except the top curve that was taken at an emission angle of 60°. The inset shows an enlarged view of the Ti 2*p* experimental spectrum with the fit results taken for 4 ML Fe at an emission angle of 60°. (b) Evolution of the Ti 2*p* core-level experimental intensity of the different titanium components obtained from spectra taken at normal emission (symbols). The intensity is plotted in semilogarithmic scale.  $I(t)$  is the integrated intensity at thickness  $t$  and  $I_{\text{Ti}^{4+}}(0)$  is the integrated intensity of the Ti<sup>4+</sup> component for the clean surface. The fitted attenuation for a layer-by-layer growth mode (continuous line) is also presented for each component.

2*p*<sub>3/2</sub> at 459.2 eV) which is characteristic of the Ti<sup>4+</sup> state. There is no evidence of components related to the Ti<sup>3+</sup> state on the clean surface. The deposition of 0.5 ML Fe leads to the appearance of a photoemission signal on the low binding energy side of the 2*p*<sub>3/2</sub> peak  $\sim 2.0$  eV away from the position of the Ti<sup>4+</sup> component that corresponds to the Ti<sup>3+</sup> component [59,60]. As the Fe coverage increases the line shape of the Ti 2*p* core-level spectrum does not change up to 4 ML where a small bump of  $-3.8$  eV relative to the Ti<sup>4+</sup> component can be detected in the photoemission spectrum. This feature corresponds to photoemission signal from titanium in an oxidation state of +2 [59,60]. Additional Fe deposition does not modify the shape of the spectra. Comparing the Ti 2*p* core-level spectra at 0° and 60° for 4 ML Fe reveals that the Ti<sup>3+</sup> and Ti<sup>2+</sup> components are contributions from titanium cations located in the near-interface region. In the inset of Fig. 6(a) is shown the Ti 2*p* core-level line shape decomposition which was performed with a least-square fitting procedure using Ti<sup>4+</sup> experimental spectrum of the clean surface as reference spectrum. To model the Ti<sup>3+</sup> and Ti<sup>2+</sup> components, this spectrum was slightly broadened and shifted in energy. The fitting procedure leads to a very good reproduction of the

experimental data that allows us to obtain the intensity of each contribution. In order to obtain the evolution of the intensities of the various components we have repeated this procedure for each of the Fe coverages. The signal, taken from photoemission spectra recorded in normal emission and divided by the Ti<sup>4+</sup> photoemission intensity of the clean surface, are plotted in semilogarithmic scale in Fig. 6(b). The intensity of the Ti<sup>4+</sup> and Ti<sup>3+</sup> components in Fig. 6(b) linearly decreases as a function of the Fe coverage with a  $1/e$  decay of  $\sim 1.2$  nm that is close to the effective attenuation length of 1.3 nm for kinetic energies of  $\sim 1.02$  keV [54] showing once more that the Fe overlayer covers uniformly the SrTiO<sub>3</sub> substrate. The Ti<sup>2+</sup> component, which is barely detectable from 4 ML Fe, has a constant intensity up to 6 ML that linearly decreases as a function of the Fe coverage with a slope similar to the other two components. These observations show again that the Fe/SrTiO<sub>3</sub> interface is formed during the deposition of the first 4–6 ML Fe and further suggest that titanium cations in +2 and +3 oxidation states are buried below the deposited iron film.

The partial reduction of the Ti oxidation state from +4 to +3 is often associated with the formation of oxygen vacancies which can be created for example by an Ar<sup>+</sup> bombardment [61], by an annealing at high temperature under low oxygen partial pressure [60], or by an intense ultraviolet irradiation [62] of the SrTiO<sub>3</sub> sample. The Ti<sup>2+</sup> valence state is related to the presence of oxygen vacancies clusters in SrTiO<sub>3</sub> [63–65]. Besides, an oxygen-deficient layer in SrTiO<sub>3</sub> can be obtained by the simple deposition of metals on a SrTiO<sub>3</sub> surface at RT [31,32,66]. By using annular-dark-field electron microscopy, Li *et al.* [32] demonstrated that, during the formation of the Ti/SrTiO<sub>3</sub>(001) interface at RT, oxygen vacancies are generated within the SrTiO<sub>3</sub> sample at several nanometers from the interface. The analysis of the electron energy-loss spectroscopy spectra at the Ti-L<sub>2,3</sub> edge reveals a significant contribution of Ti<sup>3+</sup> states in the oxygen-deficient regions. In the light of these observations our results suggest that, during the first stages of the Fe growth, the partial reduction of the Ti oxidation state is mainly caused by the diffusion of oxygen from the substrate to the overlayer. This leaves empty oxygen sites in the vicinity of the Fe/SrTiO<sub>3</sub> interface. The creation of oxygen vacancies and their rearrangements take place during the deposition of the first 4–6 ML Fe as can be inferred from the intensity variation plotted in Fig. 6(b).

In order to estimate the oxygen vacancies density within the SrTiO<sub>3</sub> substrate a simple approach is used, in particular, we assume that the reduction of the Ti oxidation state is only related to the presence of oxygen vacancies. The distribution of reduced titanium cations within the SrTiO<sub>3</sub> substrate is deduced from the analysis of the sum of the photoemission intensity of Ti<sup>3+</sup> ( $I_{\text{Ti}^{3+}}$ ) and Ti<sup>2+</sup> ( $I_{\text{Ti}^{2+}}$ ) components compared with the total intensity ( $I_{\text{total}}$ ) of the Ti 2*p* photoemission spectra for emission angles of 0° and 60° for Fe coverages higher than 6 ML. Here we are more specifically interested in the value of the ratio  $R = (I_{\text{Ti}^{3+}} + I_{\text{Ti}^{2+}})/I_{\text{total}}$ . We assume that Fe films grow in a layer-by-layer mode on TiO<sub>2</sub>-terminated SrTiO<sub>3</sub>(001) surface and that the various contributions do not show lateral inhomogeneities. To model the intensity attenuation as a function of the polar angle we

use an exponential damping factor  $\exp[-z/(\lambda \cos(\theta))]$  for photoelectrons created in depth  $z$  below the Fe/SrTiO<sub>3</sub> interface, with  $\lambda$  the effective attenuation length in the oxide ( $\lambda = 1.9$  nm in SrTiO<sub>3</sub> [54]). We compare then the experimental results with our simulation considering various configurations where the reduced titanium cations are uniformly distributed on  $n$  atomic planes of TiO<sub>2</sub> (from the interface). Considering the experimental uncertainties we find that the configurations where  $n = 1, 2$ , and 3 are possible solutions. The density of reduced titanium per surface unit deduced from this analysis is between  $3.6 \times 10^{14}/\text{cm}^2$  for  $n = 1$  and  $4.3 \times 10^{14}/\text{cm}^2$  for  $n = 3$ . The configuration where the reduced titanium cations are located only in the TiO<sub>2</sub> interface plane is unlikely. We conclude therefore that the reduced titanium cations are preferentially located in the two or three first TiO<sub>2</sub> atomic planes of SrTiO<sub>3</sub> beneath the interface with a density per surface unit of  $(4 \pm 1) \times 10^{14}/\text{cm}^2$ . Finally, we consider that each isolated oxygen vacancy donates two electrons that reduce two Ti<sup>4+</sup> cations to Ti<sup>3+</sup> cations [67,68]. Eom *et al.* [63] reported that in highly reduced SrTiO<sub>3</sub> the oxygen vacancies aggregate and tend to form linear clusters. Hence, we assume that the formation of such clusters in the TiO<sub>2</sub> atomic layers including two oxygen vacancies, which release four electrons, causes the reduction of three Ti<sup>4+</sup> cations to two Ti<sup>3+</sup> cations and one Ti<sup>2+</sup> cation.

Through this approach we find that the oxygen vacancies density at the Fe/SrTiO<sub>3</sub> interface is, on average, close to  $2 \times 10^{14}/\text{cm}^2$  and that this density is almost the same for all Fe thicknesses considered in our study. This density is very close to that of oxidized iron and confirms that oxygen atoms involved in the FeO phase are those expelled by the SrTiO<sub>3</sub> substrate during the interface formation. It is worth to mention that the appearance and the evolution of the Ti<sup>2+</sup> component as a function of the Fe thickness indicates a clustering of oxygen vacancies occurring in the vicinity of the interface for Fe layers between 0.5 and 1 nm in thickness.

Jeon *et al.* [34] found (in a first-principle calculation study) that inserting oxygen vacancies with a density of  $1.6 \times 10^{14}/\text{cm}^2$  (similar to our experimental data) in a TiO<sub>2</sub> atomic layer close to the interface of a SrRuO<sub>3</sub>/SrTiO<sub>3</sub>(001) junction reduces the SBH by more than  $\sim 0.6$  eV. This is confirmed by recent density-functional theory calculations by Ma *et al.* [35], who demonstrate that oxygen vacancies lying in SrO or TiO<sub>2</sub> atomic layers in the near-interface region of Au/SrTiO<sub>3</sub>(001) junctions also lead to the reduction of the SBH by 0.6–1 eV. This decrease depends on the interface termination and on both the position and the concentration of oxygen vacancies in the near-interface region. By taking into account these theoretical results, we conclude that the presence of oxygen vacancies at the Fe/SrTiO<sub>3</sub> interface explains the fact that the measured SBH for the Fe/SrTiO<sub>3</sub> junction ( $\sim 0.05$  eV) is far below the expected 1.3 eV calculated value [15]. According to theoretical works [34,35] the magnitude of the SBH reduction related to the vacancies insertion must be about 0.6–1 eV.

### E. Surface metallization

Another interesting point in Fig. 5 (indicated by an arrow in the figure) is that the deposition of a fraction of Fe

monolayer pushes the surface conduction band edge of the SrTiO<sub>3</sub>(001)  $\sim 0.1\text{--}0.2$  eV below the Fermi level (this value was not corrected by the band bending). This downward band bending induced by the Fe deposition implies that a fixed positive charge is created at or near the surface. The same behavior is observed no matter the doping concentrations ( $N_d$ ) used ( $5 \times 10^{18}$  and  $1.6 \times 10^{20}/\text{cm}^3$ ) or even with an undoped sample. This change in the band bending is likely to be related to the introduction of oxygen vacancies that play the role of electron donor. According to prior works, oxygen vacancies may be doubly or singly positively ionized after releasing two or one electron into the SrTiO<sub>3</sub> conduction band, respectively [33,69]. It can be noted that, in several recent works, oxygen vacancies introduction at the SrTiO<sub>3</sub> surface were believed to be responsible for the downward band bending, leading to the formation of a two-dimensional electron gas at the SrTiO<sub>3</sub>(001) surface [62,66,70]. The Fermi level being above the conduction band minimum at the surface, we expect that electrons fill the conduction band in the near-surface region giving rise to a surface electron accumulation. In bulk, the Fermi level lies 0.08 eV below the conduction band edge. This position is calculated considering that all of the donor atoms are ionized ( $N_d = 1 \times 10^{19}/\text{cm}^3$ ) and using an effective density of states in the conduction band of  $2.1 \times 10^{21}/\text{cm}^3$  [33].

We will now discuss the conduction band profile and the carrier concentration in the electron accumulation layer that we have calculated by numerically solving the one-dimensional Poisson equation within the MTFAs [36] considering parabolic bands and the anisotropy of the effective mass for electrons in the SrTiO<sub>3</sub> conduction band [71,72]. The MTFAs simulation gives results similar to that obtained through self-consistent Poisson-Schrödinger calculations but requires only a few computational resources and time [73–75]. The conduction band profile obtained through our simulations will allow us to analyze the energy shift of the Sr 3*d* core level induced by the metal deposition during the early stage of the growth.

In the bulk cubic SrTiO<sub>3</sub> the bottom of the conduction band at the  $\Gamma$  point is mainly derived from triply degenerate Ti 3*d*-*t*<sub>2*g*</sub> orbitals ( $d_{xy}$ ,  $d_{yz}$ , and  $d_{xz}$ ) [76]. The electron effective masses of the  $d_{xy}$ ,  $d_{yz}$ , and  $d_{xz}$  bands are anisotropic depending on the crystallographic directions. In the MTFAs simulation we have included the anisotropic character of the effective masses of electrons using the values taken in Refs. [70,74,77]. The *z* axis is along the direction perpendicular to the sample surface and the *x* and *y* axis are, respectively, along the [100] and [010] directions of SrTiO<sub>3</sub> crystal. The  $d_{xy}$  band has a light effective mass  $0.7m_e$  in the *xy* plane and a heavy mass  $14m_e$  along the *z* direction, where  $m_e$  is the effective mass of a free electron, whereas the  $d_{xz}$ ( $d_{yz}$ ) band has a heavy effective mass  $14m_e$  along *y* (*x*) direction and a light effective mass  $0.7m_e$  along the *z* (*z*) and *x* (*y*) directions. Finally, we took into account the electric-field and temperature dependence of the dielectric permittivity. The electric-field (*E*) dependence of the relative dielectric permittivity  $\varepsilon(E)$  is described by an empirical relationship that correctly fits the experimental data [78,79] and is given by

$$\varepsilon(E) = \frac{b}{\sqrt{a + E^2}}, \quad (1)$$

where  $a = 2.65 \times 10^{15} \text{V}^2/\text{m}^2$  and  $b = 1.42 \times 10^{10} \text{V}/\text{m}$  at RT.

The Poisson equation is self-consistently solved for a 10-nm-thick SrTiO<sub>3</sub>(001) slab using a grid of 300 regularly spaced points and setting the potential at a given value at the surface (that fixes the band bending at the surface) and at 0 V at the other end of the slab. The downward conduction band bending ( $V_{bb}$ ) is therefore an input parameter in our simulations. The surface states charge density on the semiconductor surface  $Q_{ss}$  can then be calculated using the following relation:

$$Q_{ss} = \varepsilon_0 \varepsilon(z=0) E(z=0), \quad (2)$$

where  $\varepsilon_0$  is the vacuum permittivity,  $E(z=0)$  is the electric field at the surface that is obtained from the slope of the simulated SrTiO<sub>3</sub> conduction band profile close to the surface, and  $\varepsilon(z=0)$  is the SrTiO<sub>3</sub> relative dielectric constant calculated for this electric field. The singly charged donor-type surface states density  $N_{ss}$  that causes the downward band bending is then obtained from  $Q_{ss} = qN_{ss}$ , where  $q$  is the elementary charge.

Figure 7(a) shows the calculated conduction band profiles in the near-surface region for  $N_d = 1 \times 10^{19}/\text{cm}^3$  at RT and for downward conduction band bending ( $V_{bb}$ ) of 0.30, 0.50, and 0.90 eV. In the inset of Fig. 7(a) is given the surface states density  $N_{ss}$  as a function of the downward band bending deduced from our simulations. These states are positively charged and are assumed to be related to the presence of oxygen vacancies at the surface. The curve shows a plateau for band bendings above 0.3 eV demonstrating that small variations of  $N_{ss}$  (1%–2%) around  $8 \times 10^{13}/\text{cm}^2$  yield strong changes (several tenths of an eV) of the band bending. The presence of this plateau is actually quite predictable. Indeed the surface states density is proportional to the product of the surface electric field and the value of the relative dielectric permittivity at the surface [75]. As for high electric field (higher than  $4 \times 10^8 \text{V}/\text{m}$ ) the dielectric permittivity is inversely proportional to the electric field [the constant  $a$  becomes much smaller than  $E^2$  in Eq. (1)], the surface states density must be constant whatever the value of the band bending. Thus using this simple approach we expect to observe a plateau at an  $N_{ss}$  value of  $8 \times 10^{13}/\text{cm}^2$  that is in full agreement with what we get through the simulations. It can be noted that the dielectric permittivity depends on the temperature (*T*) [78]. Indeed  $a$  and  $b$  introduced in Eq. (1) are expressed as  $b(T) = 1.37 \times 10^9 + 4.29 \times 10^7 T (\text{V}/\text{m})$  and  $a(T) = [b(T)/\varepsilon(T, E=0)]^2$ , with

$$\varepsilon(T, E=0) = \frac{1635}{\coth\left(\frac{44.1}{T}\right) - 0.937}. \quad (3)$$

This means that  $N_{ss}$  on the plateau will also depend on the temperature. More precisely we find that the  $N_{ss}$  value on the plateau decreases linearly as the temperature decreases (for example at 20 K the plateau is at  $\sim 1.2 \times 10^{13}/\text{cm}^2$ ).

An important consequence of this property is that, if the density of positively charged surface states slightly exceeds this critical value of  $8 \times 10^{13}/\text{cm}^2$  at RT, then the band bending will become very high. It follows that the electric field in the near-surface region will also be very high. As

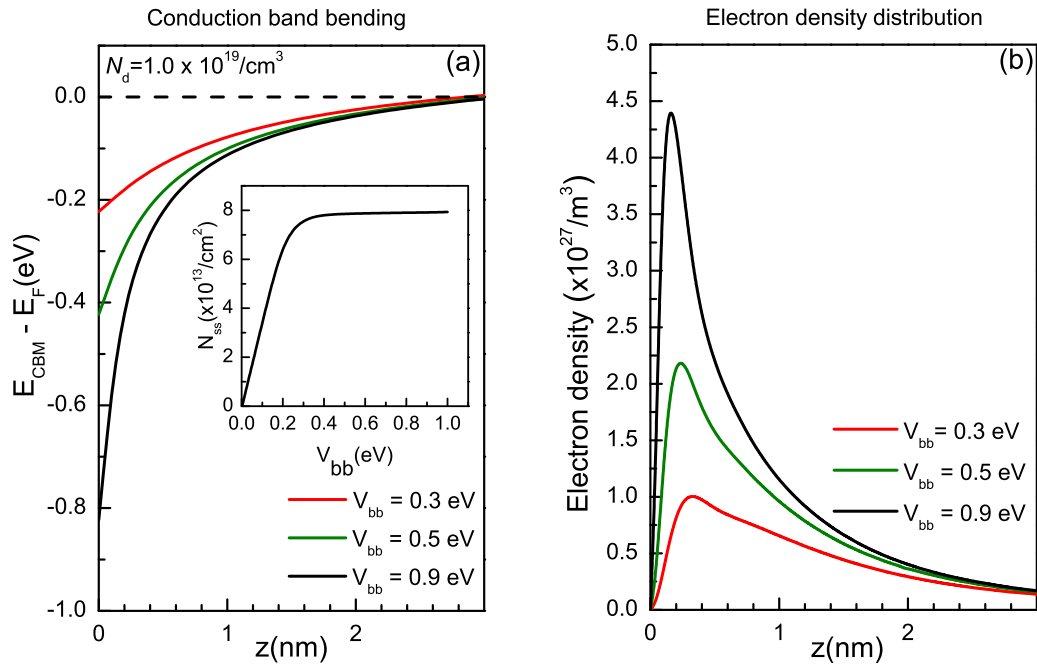


FIG. 7. (a) Energy diagram for the conduction band of SrTiO<sub>3</sub>(001) calculated along the  $z$  direction (normal to the surface) for a doping concentration  $N_{\text{d}} = 1 \times 10^{19}/\text{cm}^3$  and at RT using MTF model. The corresponding distribution of the electron densities is displayed in (b). The inset in (a) shows the evolution of surface states density  $N_{\text{ss}}$  deduced from our simulations as a function of the downward band bending  $V_{\text{bb}}$  in SrTiO<sub>3</sub>. Note the plateau for  $V_{\text{bb}}$  values higher than 0.3 eV.

a consequence, the oxygen vacancies in the surface vicinity will spread in the subsurface region or deeper into the volume through an oxygen ion migration along electric field lines [80,81]. The oxygen vacancies concentration at the surface will diminish until the surface states density takes reaches the  $8 \times 10^{13}/\text{cm}^2$  threshold value. Hence we propose that for the lowest Fe coverages, ions migration and metal oxidation mechanisms must balance each other to stabilize a surface state density less than or equal to  $8 \times 10^{13}/\text{cm}^2$  at RT.

The downward band bending leads to the formation of a narrow quantum well potential perpendicular to the sample surface in which electrons accumulate. The maximum of the electron density distribution, localized  $\sim 0.3$  nm below the surface, increases with  $V_{\text{bb}}$  [Fig. 7(b)]. Our simulations give similar results as those obtained by other groups [62,74]. From our XPS experiments we have not been able to directly obtain the carrier concentration in the surface electron accumulation layer. We observe in Fig. 7(a) that the potential variation extends over a depth ( $\sim 2$  nm) comparable to that probed by XPS. The Sr  $3d$  core-level spectra must therefore be the sum of core-level spectra, from Sr ions at different depth below the surface, but energy shifted from one SrO plane to another due to the band bending. The intensity of each contribution is weighted by an exponential damping term to take into account the attenuation of the photoelectron signal in the solid.

A layer of 10 nm of TiO<sub>2</sub>-terminated SrTiO<sub>3</sub>(001) covered by 1 ML Fe was considered to simulate the Sr  $3d_{5/2}$  core-level spectra taking into account a downward band bending ranging from 0.0 to 1.0 eV. The effective attenuation lengths of Sr  $3d_{5/2}$  core-level photoelectrons at the kinetic energy of

1.12 keV were set to 1.4 nm in Fe and 2.0 nm in SrTiO<sub>3</sub> [54]. The modulation of the photoemission intensity caused by the photoelectron diffraction effect was neglected. A Lorentzian line shape with full width at half-maximum (FWHM) of 1.0 eV was assumed to model the emission spectrum of individual Sr ions. We have found that the resulting simulated spectra resembled a Lorentzian function with an FWHM close to 1.0 eV. The resulting spectra were then fitted with a Lorentzian line shape to obtain the position of the Sr  $3d_{5/2}$  core level. We have chosen to show in Fig. 8 the variation of the kinetic energy (noted  $\Delta$  in the following) of the Sr  $3d_{5/2}$  core-level photoelectron relative to the flat band situation as a function of the band bending for emission angles of  $0^\circ$  and  $60^\circ$  (black curves in Fig. 8). The negative sign of  $\Delta$  means a downward band bending (cf. sketches in Fig. 8).

The value of  $\Delta$  experimentally obtained at normal emission for the deposition of 1 ML of Fe onto SrTiO<sub>3</sub>(001) is about  $-0.2$  eV. According to the simulations, this corresponds to a downward band bending of  $\sim 0.9$  eV. When compared with normal emission we expect that the Sr  $3d_{5/2}$  core level is shifted by  $\sim 0.08$  eV (dashed arrow in Fig. 8) towards higher binding energy at the emission angle of  $60^\circ$ . Taking into account the various source of uncertainties of our measurements, we expect that this shift is higher than 0.03 eV. Instead, no shift is detected within the experimental sensitivity (lower than 0.01 eV). Note that no detectable widening of the spectra is experimentally observed. We will see below that the absence of shift can be related to surface potential inhomogeneities.

Let us now resume our MTF simulations by introducing oxygen vacancies in the near-surface region of the slab and follow the evolution of  $\Delta$  as a function of the downward band

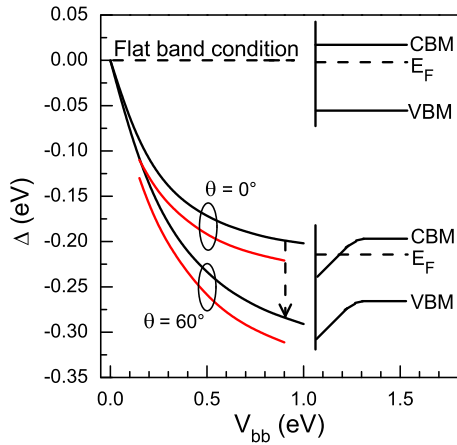


FIG. 8. Variation of the kinetic energy (noted  $\Delta$ ) of the Sr  $3d_{5/2}$  core-level photoelectron relative to the flat band situation as a function of the downward band bending for emission angles of  $0^\circ$  and  $60^\circ$ . These results are obtained from an energy diagram for the conduction band calculated within the MTF model.  $\Delta = 0$  is for the flat band condition. The calculations are performed for a doping concentration  $N_d = 1 \times 10^{19}/\text{cm}^3$  without additional vacancies in the subsurface region (black curves) and with vacancies uniformly distributed between 0.2 and 1.2 nm below the surface with a concentration of  $1 \times 10^{21}/\text{cm}^3$  (red curves). The sketches of the conduction band minimum (CBM) and valence band maximum (VBM) of SrTiO<sub>3</sub> for two different surface potentials are also shown. The dashed arrow indicates the Sr  $3d_{5/2}$  core-level shift of 0.08 eV towards lower kinetic energies expected when the emission angle  $\theta$  changes from  $0^\circ$  to  $60^\circ$  for a downward band bending of 0.9 eV.

bending. The vacancies are assumed singly charged and uniformly distributed between 0.2 and 1.2 nm below the surface with a concentration of  $1 \times 10^{21}/\text{cm}^3$  which corresponds to a density of vacancies per surface unit close to that obtained through our photoemission analysis. The doping concentration of the slab is maintained at  $1 \times 10^{19}/\text{cm}^3$  and the calculations are performed for downward conduction band bendings between 0.15 and 0.90 eV. We observe that for a given band bending the conduction band profile is very similar to that simulated without vacancies in the subsurface region. As it can be seen in Fig. 8 it follows that  $\Delta$  (red curves in Fig. 8) only slightly shifts (15–30 meV) between the two cases. The analysis of these results leads to the same conclusion that for the situation without vacancies in the subsurface region, namely that the Sr  $3d_{5/2}$  core-level position should significantly shift towards lower kinetic energies when the emission angle increases from  $0^\circ$  to  $60^\circ$ . We also observe from our MTF calculations that the band profiles shown in Fig. 7(a) are not affected, as far as the concentration of the fixed charges introduced in the SrTiO<sub>3</sub> region close to the interface ( $\sim 1$ –2 nm) is much lower than the electron concentration in the accumulation layer. Note that in these MTF calculations the surface states density  $N_{ss}$  is an output quantity obtained from the calculations while the vacancies concentration in the subsurface region is an input parameter. We have introduced a gap of 0.2 nm free of vacancies between the surface and the subsurface uniform distribution in order to maintain  $N_{ss}$

to a value close to that obtained without subsurface vacancies for the various band bendings considered in our calculations (the vacancies distribution is therefore discontinuous in the SrTiO<sub>3</sub>). Our approach is therefore not fully realistic but it gives valuable information about the impact of the presence of subsurface vacancies on the SrTiO<sub>3</sub> conduction band profile.

The surface preparation process that we have used, leads to the presence of SrO at the SrTiO<sub>3</sub> surface. We can therefore suspect that our thermal treatments favor the Sr atoms segregation at the surface that can lead to the creation of Sr vacancies within the SrTiO<sub>3</sub> substrate. As observed by Szot *et al.* [82] the Sr vacancies appear to form several hundred nanometers below the surface during this phase. Considering these results and the Sr amount that is at the surface we can estimate the mean value of the Sr vacancies concentration in the substrate. Assuming that vacancies (if they exist) are in the first 100 nm below the surface, we find that the mean vacancies concentration is about  $2 \times 10^{19}/\text{cm}^3$ . This concentration is much lower than the electron concentration in the accumulation layer obtained from our simulations [Fig. 7(a)]. We therefore expect that the presence of Sr vacancies does not change the conduction band profiles shown in Fig. 7(a).

In the inset of the Fig. 7(a) it can be seen that on the plateau a variation of  $N_{ss}$  of 1%–2% strongly affects the surface band bending. Thus we expect that a lateral change of  $N_{ss}$  of a few percent creates a spatially inhomogeneous potential at the surface. This can explain the absence of the Sr  $3d_{5/2}$  core-level spectra shift when the photoemission angle is changed. As the states relative to the oxygen vacancies are expected to be the dominant type surface states (positively charged), we propose that lateral fluctuations of the oxygen vacancies distribution are mainly responsible for the potential inhomogeneity at the surface sample. These fluctuations can come, for example, from the heterogeneous nucleation of iron cluster on the SrTiO<sub>3</sub>(001) surface during the early stage of the Fe growth or from the clustering of oxygen vacancies as proposed by Dudy *et al.* [83]. The presence of surface defects (steps, kinks, impurities, metallic clusters, SrO trenches, etc.) can also affect the surface band bending and cause surface potential fluctuations. At this stage we have too little information on the surface inhomogeneity to get the shape of the surface potential.

The oxygen vacancy concentration per surface unit estimated from the photoemission analysis in the monolayer range is  $\sim 2 \times 10^{14}/\text{cm}^2$ . Considering the different assumptions made in our study it is not reasonable to compare this concentration to the surface states density  $N_{ss}$  obtained from our MTF calculations. In fact, the quantity obtained from the MTF calculations is the fixed-charges density at the surface ( $Q_{ss}$ ). The density of surface states  $N_{ss}$  is then deduced from  $Q_{ss}$  assuming the presence of only one type of positively singly charged states (which we relate to oxygen vacancies at the surface) uniformly distributed at the surface. However, through this approach we omit to take into account the surface inhomogeneities, the possible presence of other surface states (that can be positively or negatively charged and contribute to the surface charge) due, for example, to steps, kinks, or impurities at the surface and the possible presence of oxygen vacancies in the near-surface region.

#### IV. CONCLUSION

Using XPS techniques we have conducted a detailed study on the interface formation at RT between Fe and TiO<sub>2</sub>-terminated SrTiO<sub>3</sub>(001) substrates. We observe that Fe deposition leads to the creation of oxygen vacancies within the SrTiO<sub>3</sub> lattice in the first planes beneath the Fe/SrTiO<sub>3</sub> interface. The SBH for electrons is around  $\sim 0.05$  eV giving an Ohmic behavior for electrical properties of the Fe/SrTiO<sub>3</sub>(001) contact. This low barrier height is explained by the presence of oxygen vacancies at the Fe/SrTiO<sub>3</sub> interface. The deposition of small fractions of Fe ML also drives the surface conduction band edge fairly far (higher than 0.2 eV) below the Fermi level at the surface leading to an electron accumulation layer at the surface. Solving the one-dimensional Poisson equation within the MTFM we have determined the conduction band profile and the carrier concentration in the electron accumulation layer. The SrTiO<sub>3</sub> surface, with charged surface states, exhibits interesting properties that are related to the fact that the dielectric permittivity depends on the electric field. In particular we observe that variations of a few percent of the surface states density can tremendously change (several tenths of an eV) the band bend-

ing. It follows that strong lateral potential inhomogeneities are expected from small lateral fluctuations of the surface state density as suggested by our experimental observations. Our analyses also show that for the lowest Fe coverages the defect states density related to oxygen vacancies at the SrTiO<sub>3</sub> surface cannot exceed a critical value. The surface defect states density is maintained at a value less than or equal to the critical value thanks to mechanisms such as ion migration and metal oxidation that will impact the oxygen vacancies distribution in the near-surface region. To get a deeper understanding of this particularity we are currently studying the interface formation between others reducing metals such as Mg and Al onto SrTiO<sub>3</sub>(001).

#### ACKNOWLEDGMENTS

The authors warmly acknowledge A. Le Pottier for the technical support. This work was also supported by the European Union through the European Regional Development Fund (ERDF), the French region of Brittany, and the French departmental Council of Ille & Vilaine.

- 
- [1] A. Sawa, *Mater. Today* **11**, 28 (2008).
- [2] R. Waser, R. Dittmann, C. Staiikov, and K. Szot, *Adv. Mater.* **21**, 2632 (2009).
- [3] J. J. Yang, D. B. Strukov, and D. R. Stewart, *Nat. Nanotechnol.* **8**, 13 (2013).
- [4] J. S. Lee, S. Lee, and T. W. Noh, *Appl. Phys. Rev.* **2**, 031303 (2015).
- [5] M. Yang, L. Z. Ren, Y. J. Wang, F. M. Yu, M. Meng, W. Q. Zhou, S. X. Wu, and S. W. Li, *J. Appl. Phys.* **115**, 134505 (2014).
- [6] C. Baeumer, N. Raab, T. Menke, C. Schmitz, R. Rosezin, P. Müller, M. Andrä, V. Feyer, R. Bruchhaus, F. Gunkel, C. M. Schneider, R. Waser, and R. Dittmann, *Nanoscale* **8**, 13967 (2016).
- [7] E. Mikheev, B. D. Hoskins, D. B. Strukov, and S. Stemmer, *Nat. Commun.* **5**, 3990 (2014).
- [8] N. Reyren, S. Thiel, A. D. Caviglia, L. Fitting Kourkoutis, G. Hammerl, C. Richter, C. W. Schneider, T. Kopp, A. S. Rüetschi, D. Jaccard, M. Gabay, D. A. Muller, J. M. Triscone, and J. Mannhart, *Science* **317**, 1196 (2007).
- [9] A. Ohtomo and H. Y. Hwang, *Nature (London)* **427**, 423 (2004).
- [10] A. Brinkman, M. Huijben, M. Van Zalk, J. Huijben, U. Zeitler, J. C. Maan, W. G. Van Der Wiel, G. Rijnders, D. H. A. Blank, and H. Hilgenkamp, *Nat. Mater.* **6**, 493 (2007).
- [11] C. Cen, S. Thiel, J. Mannhart, and J. Levy, *Science* **323**, 1026 (2009).
- [12] R. Arras, V. G. Ruiz, W. E. Pickett, and R. Pentcheva, *Phys. Rev. B* **85**, 125404 (2012).
- [13] Y. Zhou, Y. J. Shi, S. W. Jiang, F. J. Yue, P. Wang, H. F. Ding, and D. Wu, *Appl. Phys. Lett.* **108**, 231603 (2016).
- [14] D. C. Vaz, E. Lesne, A. Sander, H. Naganuma, E. Jacquet, J. Santamaria, A. Barthélémy, and M. Bibes, *Adv. Mater.* **29**, 1700486 (2017).
- [15] M. Mrovec, J.-M. Albina, B. Meyer, and C. Elsässer, *Phys. Rev. B* **79**, 245121 (2009).
- [16] G. W. Dietz, M. Schumacher, R. Waser, S. K. Streiffer, C. Basceri, and A. I. Kingon, *J. Appl. Phys.* **82**, 2359 (1997).
- [17] R. Schafranek, S. Payan, M. Maglione, and A. Klein, *Phys. Rev. B* **77**, 195310 (2008).
- [18] C. Capan, G. Y. Sun, M. E. Bowden, and S. A. Chambers, *Appl. Phys. Lett.* **100**, 052106 (2012).
- [19] S. A. Chambers, M. Gu, P. V. Sushko, H. Yang, C. Wang, and N. D. Browning, *Adv. Mater.* **25**, 4001 (2013).
- [20] C. Park, Y. Seo, J. Jung, and D.-W. Kim, *J. Appl. Phys.* **103**, 054106 (2008).
- [21] G. W. Dietz, W. Antpöhler, M. Klee, and R. Waser, *J. Appl. Phys.* **78**, 6113 (1995).
- [22] R. C. Neville and C. A. Mead, *J. Appl. Phys.* **43**, 4657 (1972).
- [23] T. Shimizu, N. Gotoh, N. Shinozaki, and H. Okushi, *Appl. Surf. Sci.* **117–118**, 400 (1997).
- [24] J. E. Carnes and A. M. Goodman, *J. Appl. Phys.* **38**, 3091 (1967).
- [25] D. M. Hill, H. M. Meyer, and J. H. Weaver, *J. Appl. Phys.* **65**, 4943 (1989).
- [26] K. Van Benthem and C. Scheu, *Z. Met.* **93**, 362 (2002).
- [27] Q. Fu and T. Wagner, *J. Phys. Chem. B* **109**, 11697 (2005).
- [28] Q. Fu and T. Wagner, *Surf. Sci. Rep.* **62**, 431 (2007).
- [29] Q. Fu and T. Wagner, *Surf. Sci.* **601**, 1339 (2007).
- [30] S. A. Chambers, Y. Du, M. Gu, T. C. Droubay, S. P. Heplestone, and P. V. Sushko, *Chem. Mater.* **27**, 4093 (2015).
- [31] A. B. Posadas, K. J. Kormondy, W. Guo, P. Ponath, J. Geler-Kremer, T. Hadamek, and A. A. Demkov, *J. Appl. Phys.* **121**, 105302 (2017).
- [32] Y. Li, Q. Wang, M. An, K. Li, N. Wehbe, Q. Zhang, S. Dong, and T. Wu, *Adv. Mater. Interfaces* **3**, 1600201 (2016).
- [33] R. Moos and K. H. Hardtl, *J. Am. Ceram. Soc.* **80**, 2549 (1997).

- [34] S. H. Jeon, B. H. Park, J. Lee, B. Lee, and S. Han, *Appl. Phys. Lett.* **89**, 042904 (2006).
- [35] X. Ma, Y. Dai, M. Li, and B. Huang, *Phys. Chem. Chem. Phys.* **19**, 774 (2017).
- [36] G. Paasch and H. Übensee, *Phys. Status Solidi B* **113**, 165 (1982).
- [37] G. Koster, B. L. Kropman, G. J. H. M. Rijnders, D. H. A. Blank, and H. Rogalla, *Appl. Phys. Lett.* **73**, 2920 (1998).
- [38] P. H. Citrin, G. K. Wertheim, and Y. Baer, *Phys. Rev. B* **27**, 3160 (1983).
- [39] M. Kamaratos, D. Vlachos, and S. D. Foulas, *J. Phys. Condens. Matter* **20**, 315009 (2008).
- [40] G. B. Cho, M. Yamamoto, and Y. Endo, *Sci. Technol. Adv. Mater.* **5**, 89 (2004).
- [41] T. Chien, J. W. Freeland, and N. P. Guisinger, *Appl. Phys. Lett.* **100**, 031601 (2012).
- [42] T. Yamashita and P. Hayes, *Appl. Surf. Sci.* **254**, 2441 (2008).
- [43] K. Wandelt, *Surf. Sci. Rep.* **2**, 1 (1982).
- [44] P. Schieffer, A. Guivarc'h, C. Lallaizon, B. Lépine, D. Sébilléau, P. Turban, and G. Jézéquel, *Appl. Phys. Lett.* **89**, 161923 (2006).
- [45] R. Bliem, J. Pavelec, O. Gamba, E. McDermott, Z. Wang, S. Gerhold, M. Wagner, J. Osiecki, K. Schulte, M. Schmid, P. Blaha, U. Diebold, and G. S. Parkinson, *Phys. Rev. B* **92**, 075440 (2015).
- [46] K. Mitsuhara, Y. Kitsudo, H. Matsumoto, A. Visikovskiy, M. Takizawa, T. Nishimura, T. Akita, and Y. Kido, *Surf. Sci.* **604**, 548 (2010).
- [47] N. Brookes, F. Quinn, and G. Thornton, *Vacuum* **38**, 405 (1988).
- [48] A. Pancotti, N. Barrett, L. F. Zagonel, and G. M. Vanacore, *J. Appl. Phys.* **106**, 034104 (2009).
- [49] K. Szot, W. Speier, U. Breuer, R. Meyer, J. Szade, and R. Waser, *Surf. Sci.* **460**, 112 (2000).
- [50] R. Bachelet, F. Sanchez, F. J. Palomares, C. Ocal, and J. Fontcuberta, *Appl. Phys. Lett.* **95**, 141915 (2009).
- [51] T. Matsuda, Y. Yoshida, K. Mitsuhara, and Y. Kido, *J. Chem. Phys.* **138**, 244705 (2013).
- [52] R. Bachelet, F. Sánchez, J. Santiso, C. Munuera, C. Ocal, and J. Fontcuberta, *Chem. Mater.* **21**, 2494 (2009).
- [53] R. Shimizu, K. Iwaya, T. Ohsawa, S. Shiraki, T. Hasegawa, T. Hashizume, and T. Hitosugi, *ACS Nano* **5**, 7967 (2011).
- [54] C. J. Powell and A. Jablonski, *NIST Electron Effective-Absorption-Length Database—Version 1.3* (National Institute of Standards and Technology, Gaithersburg, MD, 2011).
- [55] C. S. Fadley, R. J. Baird, W. Siekhaus, T. Novakov, and S. Å. L. Bergström, *J. Electron Spectros. Relat. Phenomena* **4**, 93 (1974).
- [56] K. Van Benthem, C. Elsässer, and R. H. French, *J. Appl. Phys.* **90**, 6156 (2001).
- [57] S. A. Chambers, M. H. Engelhard, V. Shutthanandan, Z. Zhu, T. C. Droubay, L. Qiao, P. V. Sushko, T. Feng, H. D. Lee, T. Gustafsson, E. Garfunkel, A. B. Shah, J. M. Zuo, and Q. M. Ramasse, *Surf. Sci. Rep.* **65**, 317 (2010).
- [58] P. Pal, P. Kumar, V. Aswin, A. Dogra, and A. G. Joshi, *J. Appl. Phys.* **116**, 053704 (2014).
- [59] R. Gouttebaron, D. Cornelissen, R. Snyders, J. P. Dauchot, M. Wautelet, and M. Hecq, *Surf. Interface Anal.* **30**, 527 (2000).
- [60] M. S. Martín González, M. H. Aguirre, E. Morán, M. Á. Alario-Franco, V. Perez-Dieste, J. Avila, and M. C. Asensio, *Solid State Sci.* **2**, 519 (2000).
- [61] V. E. Henrich, G. Dresselhaus, and H. J. Zeiger, *Phys. Rev. B* **17**, 4908 (1978).
- [62] W. Meevasana, P. D. C. King, R. H. He, S. K. Mo, M. Hashimoto, A. Tamai, P. Songsirittitigul, F. Baumberger, and Z. X. Shen, *Nat. Mater.* **10**, 114 (2011).
- [63] K. Eom, E. Choi, M. Choi, S. Han, H. Zhou, and J. Lee, *J. Phys. Chem. Lett.* **8**, 3500 (2017).
- [64] A. Lopez-Bezanilla, P. Ganesh, and P. B. Littlewood, *APL Mater.* **3**, 100701 (2015).
- [65] D. D. Cuong, B. Lee, K. M. Choi, H. S. Ahn, S. Han, and J. Lee, *Phys. Rev. Lett.* **98**, 115503 (2007).
- [66] T. C. Rödel, F. Fortuna, S. Sengupta, E. Frantzeskakis, P. Le Fèvre, F. Bertran, B. Mercey, S. Matzen, G. Agnus, T. Maroutian, P. Lecoeur, and A. F. Santander-Syro, *Adv. Mater.* **28**, 1976 (2016).
- [67] D. Ricci, G. Bano, G. Pacchioni, and F. Illas, *Phys. Rev. B* **68**, 224105 (2003).
- [68] X. Hao, Z. Wang, M. Schmid, U. Diebold, and C. Franchini, *Phys. Rev. B* **91**, 085204 (2015).
- [69] H. Yamada and G. R. Miller, *J. Solid State Chem.* **6**, 169 (1973).
- [70] A. F. Santander-Syro, O. Copie, T. Kondo, F. Fortuna, S. Pailhès, R. Weht, X. G. Qiu, F. Bertran, A. Nicolaou, A. Taleb-Ibrahimi, P. Le Fèvre, G. Herranz, M. Bibes, N. Reyren, Y. Apertet, P. Lecoeur, A. Barthélémy, and M. J. Rozenberg, *Nature (London)* **469**, 189 (2011).
- [71] G. Paasch and H. Übensee, *Phys. Status Solidi B* **118**, 255 (1983).
- [72] J.-P. Zöllner, H. Übensee, G. Paasch, T. Fiedler, and G. Gobsch, *Phys. Status Solidi B* **134**, 837 (1986).
- [73] H. Übensee, G. Paasch, and J. P. Zöllner, *Phys. Rev. B* **39**, 1955 (1989).
- [74] R. Yukawa, K. Ozawa, S. Yamamoto, R. Y. Liu, and I. Matsuda, *Surf. Sci.* **641**, 224 (2015).
- [75] P. D. C. King, T. D. Veal, and C. F. McConville, *Phys. Rev. B* **77**, 125305 (2008).
- [76] L. F. Mattheiss, *Phys. Rev. B* **6**, 4718 (1972).
- [77] P. D. C. King, S. McKeown Walker, A. Tamai, A. de la Torre, T. Eknapakul, P. Buaphet, S.-K. Mo, W. Meevasana, M. S. Bahramy, and F. Baumberger, *Nat. Commun.* **5**, 3414 (2014).
- [78] T. Yamamoto, S. Suzuki, K. Kawaguchi, and K. Takahashi, *Jpn. J. Appl. Phys. Part 1* **37**, 4737 (1998).
- [79] S. Suzuki, T. Yamamoto, H. Suzuki, K. Kawaguchi, K. Takahashi, and Y. Yoshisato, *J. Appl. Phys.* **81**, 6830 (1997).
- [80] J. Blanc and D. L. Staebler, *Phys. Rev. B* **4**, 3548 (1971).
- [81] J. Hanzig, M. Zschornak, E. Mehner, F. Hanzig, W. Münchgesang, T. Leisegang, H. Stöcker, and D. C. Meyer, *J. Phys. Condens. Matter* **28**, 225001 (2016).
- [82] K. Szot, W. Speier, J. Herion, and C. Freiburg, *Appl. Phys. A Mater. Sci. Process.* **64**, 55 (1997).
- [83] L. Dudy, M. Sing, P. Scheiderer, J. D. Denlinger, P. Schütz, J. Gabel, M. Buchwald, C. Schlueter, T. L. Lee, and R. Claessen, *Adv. Mater.* **28**, 7443 (2016).